PCCP

Accepted Manuscript

ROYAL SOCIETY OF CHEMISTRY

www.rsc.org/pccp

Journal Name

ARTICLE

A DFT+U study of A-site and B-site substitution in $BaFeO_{3-\delta}$

Zarah Medina Baiyee[a], Chi Chen[a] and Francesco Ciucci[a,b,†]

Received 00th January 20xx,
Accepted 00th January 20xx

DOI: 10.1039/x0xx00000x

www.rsc.org/

$BaFeO_{3-\delta}$ (BFO)-based perovskites have emerged as cheap and effective oxygen electrocatalysts for oxygen reduction reaction at high temperature. The BFO cubic phase facilitates a high oxygen deficiency and is commonly stabilised by partial substitution. Understanding the electronic mechanisms of substitution and oxygen deficiency is key to rational material design, and can be realised through DFT analysis. In this work an in-depth first principle DFT+U study is undertaken to determine site distinctive characteristics for 12.5%, Y, La and Ce substitutions in BFO. Specifically, it is shown that B-site doped structures exhibit a lower energy cost for oxygen vacancy formation relative to A site doping and pristine BFO. This is attributed to the stabilisation of holes in the oxygen sub-lattice and increased covalency of the Fe-O bonds of the FeO_6 octahedra in B-site-substituted BFO. Charge analysis shows that A-site substitution amounts to donor doping and consequently refrains the accommodation of other donors (i.e. oxygen vacancies). However, A-site substitution may also exhibit a higher electronic conductivity due to less lattice distortion for oxygen deficiency compared to B-site doped structures. Furthermore, analysis of the local structural effects provides physical insight into stoichiometric expansions observed for this material.

1. Introduction

Energy security and climate change are amongst the most pressing issues faced by the world today, with the development of renewable and sustainable energy becoming essential to building a secure and environmentally conscious future.[1] Solid oxide fuel cells (SOFCs) are one of the most promising energy conversion technologies due to their high efficiency and fuel flexibility.[2-4] The high operating temperatures of SOFCs, typically between 800°C and 1000°C, lead to component degradation and challenging thermal management.[5] These challenges can be resolved by lowering the SOFC operating temperatures to the 500°C-800°C range. However, for lower temperature operation oxygen reduction reactions become sluggish. To overcome this behaviour, mixed ionic and electronic conductors (MIECs) have been used to extend the electrochemically active area beyond the triple phase boundary.[6] Among the various MIECs, perovskite-structured materials of the form ABO_3 (A is a lanthanide or alkaline earth element and B is transition metal) have gained significant attention. This interest can be attributed to their ability to accommodate different A and B site cations and allow substitution of various elements. These features enable fine-tuning of material properties including electronic and ionic conductivity, and catalytic activity. The ability to calibrate perovskite properties has also lead to the recent interest in their application for photovoltaic solar cells.[7, 8] Barium-based perovskites, such as $Ba_{0.5}Sr_{0.5}Co_{0.8}Fe_{0.2}O_{3-\delta}$[9], $Ba_{0.6}La_{0.4}CoO_{3-\delta}$[10], $BaCo_{0.7}Fe_{0.3-x}NbO_{3-\delta}$[11], $Ba_{0.5}Sr_{0.5}Zn_{0.2}Fe_{0.8}O_{3-\delta}$[12], $BaCe_xFe_{1-x}O_{3-\delta}$[13] etc., have exhibited several promising features for SOFC applications, including high oxygen deficiencies up to δ~0.64 at 700°C and a pO_2 of 1 atm for $Ba_{0.5}Sr_{0.5}Co_{0.8}Fe_{0.2}O_{3-\delta,}$[14] with large lattice volumes due to the large ionic radius of Ba^{2+}.[15, 16] On the other hand B-site cations in perovskite oxides are generally regarded as the active site for electrochemical catalytic activity, with Co-based perovskite oxides demonstrating outstanding activity at lower temperatures 600°C -850°C.[9, 17, 18] Several challenges, including the high material costs, have limited the application of these promising materials.[16, 19] This has resulted in an increased interest in cobalt-free perovskite, such as $BaFeO_{3-\delta}$ (BFO). BFO exhibits several promising properties, including high oxygen deficiency for the cubic phase.[20] However for solid state and sol-gel methods of synthesis, BFO may also form a hexagonal structure at lower temperatures, limiting oxygen permeability.[20, 21] Although a recent study demonstrated the successful fabrication of the cubic phase for low temperature (200°C) upon oxidation in ozone, this structure also exhibited a high oxygen site occupancy.[22] The stabilization of the cubic structure and the high oxygen deficiency has also been obtained by substituting Sr, Ce, La, Y, Ca [16, 21, 23-27] into the A-site or Nb, Y, Ce, Zr, Ni, Cu[28-32] into the B-site. Several of these materials have demonstrated improved oxygen permeability in comparison to the pristine BFO.[27] They have also shown improved electronic and ionic conductivities, operational

[a] Department of Mechanical and Aerospace Engineering, The Hong Kong University of Science and Technology, Hong Kong, China
[b] Department of Chemical and Biomolecular Engineering, The Hong Kong University of Science and Technology, Hong Kong, China
[†] Corresponding author: francesco.ciucci@ust.hk
Electronic Supplementary Information (ESI) available: [details of any supplementary information available should be included here]. See DOI: 10.1039/x0xx00000x

stability, and cell performances comparable to cobalt-based cathodes.[16, 21]

Although the strategy of stabilizing BFO by substitution is commonly employed, significant ambiguity exists as to the electronic and geometric effects of each site doping. An example is the unclear structural effect of substitution site, this is highlighted in recent studies of 5% doping of Ce_{Ba} [21] and Ce_{Fe}[32], where a very similar lattice constant was reported a=b=c= 4.04Å and a=b=c= 4.035Å respectively. In addition, other studies have identified different structural and crystal characteristics for the same materials, for example, an oxygen deficiency of δ=0.27[27] (for iodometry at 930°C) and δ=0.38[25] (for iodometry at room temperature) for La_{Ba} at 10% substitution level. Most often the substitution location (A site or B site) is determined from the initial stoichiometry of the material constituents and analysis of XRD data. [16, 21, 24, 25, 27, 29-33] Stoichiometric expansion with substitution level is also employed to validate the substitution location.[25, 27, 32] In relation to this, a recent review by Bishop et al[34] discussed the complexity of the inter-correlated factors driving perovskite lattice expansion, including subtle crystal structure changes, transition metal spin states, cation site, charge localisation, and oxygen stoichiometry.[35] Moreover, for other Fe-based perovskites ($La_{0.3}Sr_{0.7}FeO_{3-\delta}$), the stoichiometric expansion due to oxygen deficiency was experimentally found to be up to 5% at 900°C.[36] As doping may also influence the oxygen deficiency in BFO, it is essential to develop a more detailed understanding of the geometric impact of oxygen vacancies.

Recently, several DFT studies have been employed to model perovskite materials and identify the factors that influence the electronic and ionic conductivities, the electronic structure, the surface properties and the surface termination.[37-42] Several of these studies identified the impact of substitution on the crystal structure and on the electronic density, and elucidated atomistic level mechanisms of crystal properties, such as oxygen vacancy formation as an indicator for deficiency, orbital hybridisation, and electronic conductivity. Furthermore, the oxygen vacancy formation energy indicator has also been strongly correlated to the performance of SOFC perovskite electrodes.[43] This is due to the perovskite oxide mechanism of diffusion via oxygen hopping facilitated by vacancy sites.[44]

Although detailed DFT studies have been undertaken for other Fe based perovskites, including $LaFeO_{3-\delta}$, $La_{1-x}Sr_xFeO_{3-\delta}$, $La_{1-x}Sr_xCo_{1-y}Fe_yO_{3-\delta}$, $Sr_2FeMoO_{6-\delta}$, and $Ba_{0.5}Sc_{0.5}Co_{0.8}Fe_{0.2}O_{3-\delta}$, no similar study has been undertaken on BFO and its single site derivatives, until now.[37, 39, 44-47] This study aims to bridge the gap in literature and employ DFT+U analysis methods to identify the electronic and geometric mechanisms of substitution, oxygen deficiency, and conductivity for A-site and B-site substituted BFO.

As BFO has demonstrated improved performance for both A-site and B-site substitutions, this work aims to clarify the effect of each site doping. The trends and traits identified are suggested as additional keys to help in the rational design and development of this material. This study examines the substitution of elements of Y, La and Ce, for both A_{Ba} and B_{Fe} separately (going forward, A-site substituted BFO is referred to as A_{Ba}, and B-site substituted BFO as B_{Fe}). Furthermore, as Y and La have the same common oxidation state of 3+, the effect of other characteristics, such as ionic radii and electronegativity, is also examined.

2. Methodology and Computational Details

To investigate the structural, electronic and magnetic properties of A_{Ba} and B_{Fe} defects in BFO, a first principles DFT study was undertaken, using projected augmented waves (PAW) with the PBE, GGA+U type exchange correlation as implemented in the VASP code.[48, 49] The kinetic energy cut-off for the plane wave basis set was set to 480eV, using a 6x6x6 Monkhorst-Pack grid,[50] for an energy convergence within 3meV per unit cell. PAW-PBE pseudopotentials were employed for Ba ($5s^25p^66s^2$), Fe ($3p^63d^74s^1$), La ($5s^25p^66s^25d^1$), Ce ($5s^25p^66s^25d^14f^1$), Y ($4s^24p^65s^24d^1$) and O ($2s^22p^4$).[51] A Hubbard-model was employed to account for the localised 3d and 4f electrons of Fe and Ce respectively. A U_{eff} parameter of 4eV was included for Fe, and 5.3eV for Ce, as derived from previous work on structural and electronic properties of Fe based perovskite oxides[43] and CeO_2 and Ce_2O_3 oxides.[52]

Spin-polarised calculations were performed with four types of magnetic configurations, FM, A-AFM, C-AFM and G-AFM. Initially the cubic $Pm\bar{3}m$ perovskite 2x2x2 supercells were relaxed to determine the lattice parameters for BFO and the A and B site substituted materials. Next, full internal ionic relaxations were performed to allow local distortions and determine the ground state electronic, magnetic, and structural properties.[43]

The 40 atom supercells enabled a minimum substitution level of 12.5%, with separate A_{Ba} and B_{Fe} defects of BFO studied for all elements. Thus the cubic perovskite materials, $BaFeO_3$, $Ba_{0.875}La_{0.125}FeO_3$ (La_{Ba}), $BaFe_{0.875}La_{0.125}O_3$ (La_{Fe}), $Ba_{0.875}Ce_{0.125}FeO_3$ (Ce_{Ba}), $BaFe_{0.875}Ce_{0.125}O_3$ (Ce_{Fe}), $Ba_{0.875}Y_{0.125}FeO_3$ (Y_{Ba}), and $BaFe_{0.875}Y_{0.125}O_3$ (Y_{Fe}) were studied. To date La_{Fe} has not been experimentally confirmed for sole cubic stabilisation of BFO, however it has been in conjunction with Zr, i.e., $BaFe_{0.91}La_{0.04}Zr_{0.05}O_{3-\delta}$ and $BaFe_{0.925}La_{0.025}Zr_{0.05}O_{3-\delta}$,[53] therefore it is presently included in a predictive capacity only. Although most experimental studies of these materials suggest an optimum 5% substitution level, the 12.5% level of doping has been employed to conduct an efficient comparative analysis between the two sites.

The DFT+U model was employed to identify the energy cost of forming oxygen vacancies and to determine the electron redistribution, for both A_{Ba} and B_{Fe} substitution in BFO. The defect formation energies are determined as the energy difference (E_{form}) between the defective (E_{def}) and perfect (E_p) crystal structure, plus the chemical potential of the initial atom μ_i and minus the chemical potential of the substitute μ_s:

$$E_{form} = E_{def} - E_p + \mu_i - \mu_s \quad (1)$$

The chemical potential of the substitute is calculated from the potential of its oxide, this is consistent with oxygen rich fabrication conditions.[39] A similar approach was employed to

compute the energy cost for the formation of oxygen vacancies E_{vac}:[37]

$$E_{vac} = E_{def,v} - E_p + 1/2(\Delta h_o + \mu_{O_2}) \quad (2)$$

where $E_{def,v}$ corresponds to the energy of the vacancy defective structure. An O_2 overbinding correction term (Δh_o) was calculated at 1.4eV for triplet O_2 and μ_{O_2} and corresponds to the chemical potential of an O_2 triplet.[54]

3. Results and discussion

3.1 Oxygen Deficiency

For substituted materials the cubic perovskite structures facilitate several unique oxygen vacancy sites, dependent on vacancy position relative to the substitute. These unique oxygen sites are outlined in Figure 1: oxygen sites directly coordinating either the A_{Ba} or B_{Fe} defects are noted as O_{NN} (nearest neighbours); oxygen sites in the second sphere of coordination of the defects are indicated as O_{2NN} (the second nearest neighbours); for B_{Fe} substitution a third sphere of coordinated oxygen sites is noted as O_{3NN} (third nearest neighbours). The average energy of oxygen vacancy formation across all vacancy sites, for all A_{Ba} and B_{Fe} defects is shown in Figure 2. A first observation is the low energy cost of oxygen vacancies, for both site defects. It is however difficult to compare these results with other DFT studies of materials, such as $Ba_{0.5}Sr_{0.5}Co_{0.75}Fe_{0.25}O_{3-\delta}$ (1.34eV-1.4eV),[45] where the Hubbard U approximation is not included. Previous studies have found that this U parameter strongly impacts the energy of oxygen vacancy formation.[55] Here, the low energy of oxygen vacancy formation calculated for BFO and A_{Ba} and B_{Fe} defects, may be attributed to the high Ba content, indeed the oxygen deficiency of $Ba_{1-x}Sr_xCo_{1-y}Fe_yO_{3-\delta}$ has shown a dependency on Ba stoichiometry.[56] This suggests a high oxygen deficiency for these materials, which is in agreement with experimental observations.[16, 21, 24, 25, 30, 32, 33] This finding is also supported by a high oxygen deficiency of La_{Ba}, which has been related to the high cathode ORR performance in $Ba_{0.95}La_{0.05}FeO_{3-\delta}$-based fuel cells, comparable to cobalt-based $La_{0.6}Sr_{0.4}Co_{0.2}Fe_{0.8}O_{3-\delta}$ and $Sm_{0.5}Sr_{0.5}CoO_{3-\delta}$.[16] Figure 2 also clearly shows that B_{Fe} defects exhibit a lower energy cost for oxygen formation relative to A_{Ba} defects for all elements. As the formation of an oxygen vacancy is equivalent to adding two electrons to the crystal, the electronic structure of the material and the mechanisms employed to accommodate this additional charge is key. Therefore, these properties were explored beginning with the BFO ground state in order to validate the DFT+U model employed.

3.2 BFO Ground State Structure

Table 1 shows the geometric, magnetic and electronic properties calculated for the BFO cubic perovskite. The lattice constant and Fe magnetic moment are in good agreement with the experimental stoichiometric BFO $Pm\bar{3}m$ structure at room temperature.[22] The inclusion of the Hubbard-U term for the self-interaction of the localised Fe 3d electrons greatly improves the Fe spin ordering from 3.01μ_B to 3.87μ_B, a value closer to the experimental result of 3.5μ_B.[22] However, the inclusion of this term also leads to an overestimation of the lattice volume, and increases the lattice parameter from 3.97Å (GGA). As the primary focus of this work was to investigate the quantum process of electron localisation in oxygen vacancy formation, accurate spin ordering was considered most imperative, and therefore the Hubbard-U approximation was included. The FM spin state was identified as the ground state, this is consistent with previous DFT+U studies of parallel magnetic orderings of cubic BFO and SOFC operating conditions.[43, 57] However, experimental analysis of the cubic stoichiometric BFO, identified an A-AFM type spin-spiral state below 111K, and FM above.[22] In relation to this, other DFT work studied a more precise helical spin ordering and found an

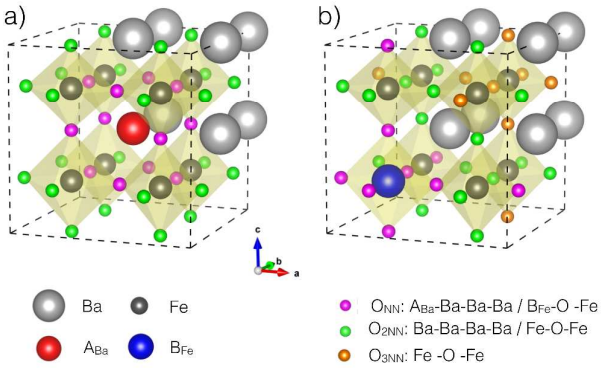

Figure 1. Distinct oxygen sites for A_{Ba} and B_{Fe} structures: a) A_{Ba} structure with unique oxygen sites; O_{NN} directly coordinated by the A_{Ba} defect in A-Ba-Ba-Ba; and O_{2NN}, of oxygen atoms not coordinated by the A_{Ba} defect, Ba-Ba-Ba-Ba, b) B_{Fe} structure with three unique oxygen sites; O_{NN} in the B_{Fe}-O-Fe chain; O_{2NN} in the second sphere of coordination to the B_{Fe} defect in an Fe-O-Fe chain; O_{3NN} in the third sphere of coordination to the B_{Fe} defect in an Fe-O-Fe chain.

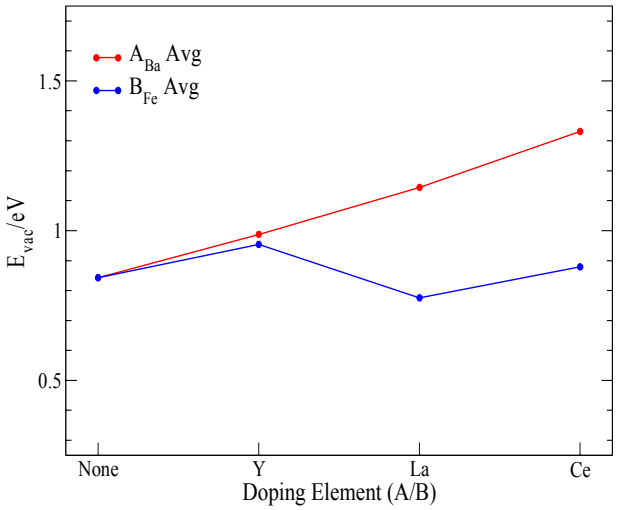

Figure 2. Energy required for oxygen vacancy formation for parent BFO and with A_{Ba} and B_{Fe} substitutions. For A_{Ba} and B_{Fe}, the average formation energy for all distinct vacancy sites is shown, as is Figure 1.

Table 1. Experimental and calculated lattice constant, $a=b=c$ (Å), and magnetic moment of Fe μ_{Fe} (μ_B), for cubic BFO, A_{Ba} and B_{Fe} substituted structures. For experimental reference, parenthesis corresponds to substitution level.

Structure	a (DFT+U)	a (Exp.)	μ_{Fe}
BFO	4.013	3.97[22]	3.87
Y_{Ba}	3.990	---	3.88
Y_{Fe}	4.071	~4.05[30] *(12.5%)*	3.79
La_{Ba}	3.999	4.01[27] *(10%)*	3.88
La_{Fe}	4.087	---	3.78
Ce_{Ba}	3.999	4.035[21] *(5%)*	3.92
Ce_{Fe}	4.095	4.096[32] *(15%)*	3.77

almost degenerate A-AFM and G-AFM ground state. [58] However, the same study also identified a small energy barrier (0.017 meV per unit cell) for the transition from AFM to FM structures. This supports the FM ordering considered here.

Next, the electronic structure of BFO was explored in the projected density of states (PDOS), Figure 3, which revealed a nearly half-metallic electronic structure with a high Fe spin state; this is consistent with previous DFT+U studies. [57, 58] The deep energy of the Fe 3d majority bands and the dominance of the O 2p bands at the Fermi level suggest a metal to ligand charge transfer.[57] Based on this, the O 2p states at the Fermi-level and above are considered hole-type. This is compatible with previous experimental work, which suggests a ligand hole $Fe^{3+}L$ (L: ligand hole) structure for the stoichiometric BFO[16] and other experimental observations of BFO (and some derivatives) as a p-type semi-conductor.[21, 24] Furthermore, this hole structure was also theoretically clarified by an oxygen self-doping mechanism for the non-stoichiometric $BaFeO_{2.5}$ to $BaFeO_3$.[22, 57]

3.3. Effect of Substitution

The effect of site substitution was then explored by analysing the ground states of the A_{Ba} and B_{Fe} substituted BFO materials, with FM spin ordering considered for all structures. As a result of the different bonding coordination and consequent valence states of the A and B sites in perovskite oxides, a different electronic effect for each site doping is expected. Simple charge conservation of the pristine BFO suggests an initial Ba^{2+} and Fe^{4+} oxidation state. However, as discussed above, a Fe^{3+} oxidation state is considered to facilitate ligand holes in the oxygen sub-lattice. Based on this, it is expected that the substitution of Y^{3+}, La^{3+} and $Ce^{3+/4+}$ on the Ba^{2+} site (A_{Ba} defects) may amount to donor doping. Furthermore, the negative charge introduced by donor doping may be facilitated by recombination with the oxygen ligand holes or the reduction of the Fe cations. The same substitution of the Fe^{3+} site (B_{Fe} defects) may result in charge redistribution or structural modifications only, with no net charge to the lattice. To explore this effect, a topological analysis of charge re-ordering was undertaken using the Bader charge model[59-61] for the parent BFO and A_{Ba} and B_{Fe} substituted structures as shown Table 2. For all structures, the covalent nature of the bonds is revealed by the lower Bader charges than the expected oxidation state.

For A_{Ba} defects, the defect site exhibits an increased Bader charge, which is balanced by a localisation of negative charge to the oxygen sub-lattice, for all substitute elements. As expected this is consistent with the donor doping heuristic argument given above. Furthermore, the localisation of the donor electron in the oxygen sub-lattice suggests that the O 2p ligand hole states withdraw this charge. This is verified by the analysis of the PDOS of the La_{Ba} substituted structure, which shows a clear shift in the Fermi level to a higher energy, see Figure 3, indicative of donor doping. To note, in Figure 3 only the La_{Ba} and La_{Fe} PDOS are displayed, yet similar trends are observed for all defects (Figure S1). In addition, there is little change to the charge and spin state (μ_{Fe}) of the Fe cations for all types of A_{Ba} substitution. This suggests that the Fe cations are screened by the oxygen sub-lattice. Table 2 also outlines the structural effect of substitution. For all A_{Ba} defects, a negligible Fe-O bond expansion and oxygen displacement is observed. This minimal structural effect of A_{Ba} doping, given

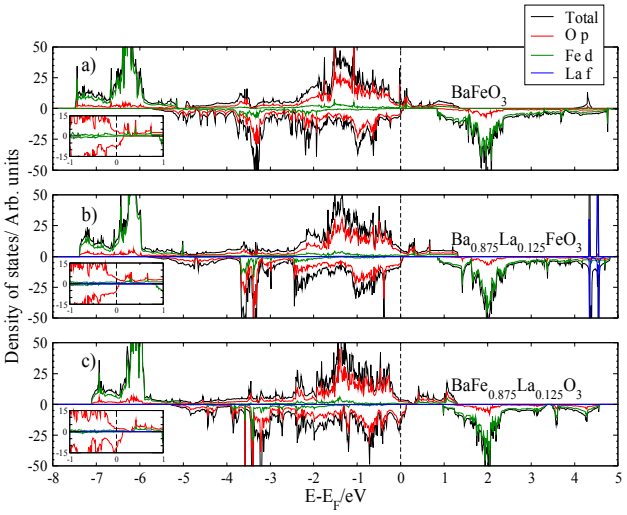

Figure 3. Projected Fe, O & La, and total density of states of a) BFO b) with La_{Ba} defects c) with La_{Fe} defects. The vertical dashed lines correspond to the Fermi Energy and insets show Fermi-level detail. Positive PDOS values correspond to spin up channel, and negative values correspond to spin down channel

Table 2. Magnetic moment for Fe, μ_{Fe} (μ_B), Bader charge per atom, q (e) where $q_{A/B}$ corresponds to defect charge, average B-O bond length, *B-O*(Å) and oxygen site displacement relative to mid-position, z (Å), for BFO, A_{Ba} and B_{Fe} substituted structures.

	BFO	Y_{Ba}	La_{Ba}	Ce_{Ba}	Y_{Fe}	La_{Fe}	Ce_{Fe}
μ_{Fe}	3.87	3.88	3.88	3.92	3.79	3.78	3.77
q_{Fe}	1.84	1.83	1.85	1.83	1.70	1.66	1.74
q_{Ba}	1.58	1.58	1.60	1.59	1.59	1.59	1.57
q_O	-1.14	-1.17	-1.18	-1.16	-1.11	-1.11	-1.12
$q_{A/B}$	---	2.21	2.19	2.20	2.12	2.19	2.26
B-O	2.00	2.00	2.00	2.00	2.04	2.05	2.05
z O_{NN} [a]	---	-0.01	0.00	0.00	0.18	0.24	0.19
z O_{2NN} [a]	---	0.01	0.00	0.00	0.06	0.06	0.08
z O_{3NN} [a]	---	---	---	---	0.05	0.06	0.15

[a] *z*, positive displacement corresponds to displacement away from the defect and negative corresponds to direction towards the defect.

the large difference in ionic radii (Y^{3+}: 0.9 Å, La^{3+}: 1.032 Å & Ce^{3+}: 1.01 Å),[62] suggests that the A_{Ba} substitution considered have a limited effect on the FeO_6 octahedra in BFO.

Unlike A_{Ba} defects, B_{Fe} substitution results in charge redistribution and geometric restructuring throughout the lattice, see Table 2. Firstly, similar to A_{Ba} defects, B_{Fe} defects also exhibit an increased charge relative to the Fe cations in BFO. However, the gain of charge of the B_{Fe} site is much less compared to the A_{Ba} sites in A_{Ba} substitution. Nonetheless, this suggests an increased ionic strength of the B_{Fe}-O bonds, relative to the original Fe-O, and can be rationalised by the increased electronegativity mismatch (Y: 1.2, La: 1.1, Ce: 1.12 & Fe: 1.8).[62, 63] This is further supported by a restructuring of the B_{Fe}-coordinated oxygen anions (O_{NN}), which undergo a significant displacement away from the B_{Fe} defect. The magnitude of this displacement correlates well with the ionic radii (Y^{3+}: 0.9 Å, La^{3+}: 1.032 Å & Ce^{3+}: 1.01 Å, the similar charge reorganisation to Y^{3+} and La^{3+}, suggests an Ce^{3+} state).[62, 63] Therefore, both the electronegativity and ionic radii of the defect influence the nature of the B_{Fe}-O bonds.

The introduction of B_{Fe} defects also perturb both the structure and bonding throughout the lattice. Firstly, the charge introduced at the defect site is balanced by a reduction of the Fe cations and the simultaneous localisation of positive charge onto the oxygen sub-lattice. Secondly, the defect ionic radii mismatch produces significant restructuring of the FeO_6 octahedra throughout the lattice, resulting in flattening and lengthening of adjacent octahedra and an overall Fe-O bond expansion. These combined effects indicate an overall increase in covalency of the Fe-O bonds. Therefore, unlike A_{Ba} defects, B_{Fe} defect charge reorganisation has little effect on the O 2p band hole structure of the parent BFO. This is also confirmed by PDOS analysis of the La_{Fe} doped structure, as shown in Figure 3.[22]

For B_{Fe} substitution, as only a small charge addition to the lattice is observed, it is concluded that Y^{3+}, La^{3+} and Ce^{3+} replace an initial Fe^{3+} cation, as expected.[22, 57, 64] This suggestion is also supported by the analysis of the spin state of Fe with B_{Fe} substitution, as shown in Table 2. Here, a localisation of negative charge to the Fe cations produces a concurrent drop in the Fe magnetic moment (μ_B), for all substitutes. Based on a high Fe spin state and spin ordering, the reduction in μ_B also indicates an initial approximate Fe^{3+} oxidation state.

3.4. Site Distinct Electronic Mechanisms of Oxygen Vacancy Formation

As outlined above, A_{Ba} and B_{Fe} doping produce different charge redistribution and restructuring of the BFO lattice, which may be responsible for the lower oxygen vacancy formation in B_{Fe} over A_{Ba} structures. This is confirmed by Bader charge analysis, as in Table 3. It should be noted that, only La substitutions are presented as La substitution has attracted much interest due to a promising performance and similar trends are observed for all doped elements (Table S1).[16, 24-27, 53] Here for the formation of an oxygen vacancy, a clear dominant charge accommodation in the oxygen sub-lattice is observed for the La_{Fe} structure. Whereas, for the La_{Ba} structure, the additional charge is primarily accommodated by the reduction of the adjacent Fe ions, the La_{Ba} substitute and a small reduction of charge in the oxygen sub-lattice.

Table 3 shows a correlation between the vacancy formation energy and the amount of donor charge accommodated in the oxygen sub-lattice, La_{Fe}>BFO>La_{Ba}. This finding can be rationalised by considering the previously outlined effects of doping. For B_{Fe} substitution the increased covalency and

Table 3. Difference in properties relative to the oxygen stoichiometric structures: Bader charge $q(e)$, where $q_{LaBa/LaFe}$ corresponds to defect charge, Magnetic moment of Fe $\mu_{Fe}(\mu_B)$, vacancy adjacent bond expansion *Fe*-O-Fe** (*Å*) and *B-O-B* channel torsion (^{o}) for the stoichiometric structures of BFO and BFO with La_{Ba} and La_{Fe} defects relative to the stoichiometric structure for oxygen deficiencies: δ =0.125, 0.25 & 0.375. The energy of formation per oxygen vacancy E_{vac} (eV) is also shown.

	BFO	La_{Ba}			La_{Fe}		
Property	δ = 0.125	δ = 0.125	δ = 0.25	δ = 0.375	δ = 0.125	δ = 0.25	δ = 0.375
$\Delta\ \mu_{Fe}$	0.11	0.13	0.33	0.31	0.09	0.20	0.27
$\Delta\ \mu_{Fe*}$ [a]	-0.28	-0.19	0.19	0.23	-0.24	0.04	0.17
$\Delta\ q_{Fe}$	-0.02	-0.03	-0.06	-0.08	0.09	0.08	0.04
$\Delta\ q_{Fe*}$ [a]	-0.15	-0.16	-0.15	-0.16	0.09	0.06	0.04
$\Delta\ q_{Ba}$	-0.01	-0.04	-0.06	-0.07	-0.03	-0.04	-0.05
$\Delta\ q_{LaBa/LaFe}$	---	-0.09	-0.12	-0.13	-0.06	-0.12	-0.18
$\Delta\ q_O$	-0.03	-0.01	-0.05	-0.09	-0.06	-0.1	-0.14
Δ *Fe*-$V_o^{\bullet\bullet}$-Fe** [b,c]	0.27	0.20	0.27	0.25	0.30	0.26	0.28
Δ *B-O-B* [d]	---	4.3	5.5	5.6	1.1	5.1	9.7
E_{Vac} *per O* [e]	0.86	1.14	1.34	1.75	0.78	1.00	1.22

[a] Fe* indicates the Fe ions adjacent to the vacancy. [b] $V_o^{\bullet\bullet}$ in Kröger-Vink notation [c] Fe*- $V_o^{\bullet\bullet}$-Fe* corresponds to Fe-Fe distance for the additional vacancy site only. [d] Average torsion determined from absolute angle relative to 180^o for cubic B-O-B, along each channel. [e] For δ = 0.125 corresponds to average energy for vacancy sites, for δ > 0.125, the lowest energy vacancy site for the lower δ is used as a basis, and the formation energy corresponds to average energy for all site combinations with this basis.

hybridisation in the FeO_6 octahedra facilitate a better delocalisation of the vacancy donor charge to the ligand holes in the oxygen sub-lattice. Whereas for the BFO structure, less donor charge is accommodated by the hole states, with a significant proportion reducing the Fe cations. This can be attributed to the lower covalency in Fe-O in BFO in comparison to B_{Fe} structures, and hence more reducible Fe. A similar charge redistribution for oxygen vacancy formation as BFO, is observed for La_{Ba} structures, however with less charge to the oxygen lattice. The lower accommodation of charge to the oxygen sub-lattice in La_{Ba} can be rationalised by considering the effect of A_{Ba} substitution as donor doping, leading to a reduction in oxygen hole states and impeding the further accommodation of donor charge.

In both BFO and B_{Fe}, the donor charge localisation in the Fe lattice produces a concurrent drop in the Fe magnetic moment. This may indicate a transition of the high spin Fe^{3+} to Fe^{2+}, resulting in anti-parallel spin ordering of the Fe 3d electrons. The interelectronic Coulombic repulsion associated with this ordering introduces an additional energy barrier in oxygen vacancy formation. This may also be associated with an increase in crystal field splitting energy as a result of the perturbation to the oxygen ligand octahedra. As a consequence, more Fe 3d electrons localise in the lower energy t_{2g} orbitals, reducing the magnetic moment and creating a similar additional energy barrier associated with anti-parallel spin ordering. Both suggestions are supported by the higher formation energies of A_{Ba} and BFO in comparison to B_{Fe}. This Coulombic repulsion has previously been identified as a contributor to high energy of vacancy formation for other Fe-based perovskites.[37, 44, 61]

In addition to this, the reduced accommodation by the oxygen lattice in La_{Ba} structures results in the significant localisation of charge to the less reducible A cations throughout the rest of the lattice. This is particularly interesting and suggests the reducibility of the A_{Ba} defect may also influence the oxygen vacancy formation energy. This observation is consistent with the correlation between the ionisation potential of A_{Ba} (Y^{3+}>La^{3+}>Ce^{3+})[65] and the oxygen vacancy formation energy. This may be also rationalised by noting that a larger potential corresponds to a more exothermic reduction of the A_{Ba}^{3+} to A_{Ba}^{2+}, hence lowering the vacancy formation energy.[61]

Figure 4 shows the oxygen vacancy formation energy for the best (lowest energy) and worst (highest energy) oxygen sites fro A_{Ba} and B_{Fe} structures. This shows a common low energy oxygen vacancy site for all elements for each A_{Ba} and B_{Fe} substitution. For A_{Ba} defects, the low energy vacancy position (O_{NN}) is coordinated by the A_{Ba} substitute, which is consistent with previous DFT findings of favourable vacancies coordinated by La^{3+} in comparison to Sr^{2+}.[46] As only a small energy difference (ΔE_{vac}=0.2-0.4 eV) between the two unique vacancy sites is observed, both are expected to exist. Moreover, this similar energy for different vacancy sites indicates a delocalised character for the charge redistribution following vacancy formation in A_{Ba} structures. This is depicted in the electron density difference plots, Figure 5(a-c). Here, for all A_{Ba} substituted elements, charge redistribution across the whole lattice is observed, including Fe cations and O anions not coordinated by the vacancy. For B_{Fe} substitution the formation of oxygen vacancies strongly depends on the vacancy position relative to the defect. This is also depicted in Figure 5(d-g), with more localised charge redistribution similar to BFO.

For all B_{Fe} doped materials, the defect-coordinated sites (O_{NN}) exhibit the highest energy for oxygen vacancy formation. As a consequence it is not expected for these sites to contribute to the B_{Fe} oxygen deficiency. The high energy of the B_{Fe} O_{NN} sites, can be attributed to the increased ionic strength of the B_{Fe}-O_{NN} bonds. Indeed, this is supported by a correlation between the gain in charge of the B_{Fe} cation (La<Y<Ce) and the oxygen vacancy formation energy of O_{NN} (La<Y<Ce).

Interestingly, the B_{Fe} O_{2NN} sites exhibit the lowest energy for oxygen vacancy formation compared to all A_{Ba} vacancy sites and BFO. It is therefore expected that the O_{2NN} sites will dominate the B_{Fe} structures. Moreover, the low energy of the O_{2NN} may increase the B_{Fe} oxygen deficiency in comparison to equivalent A_{Ba} substitution and the pristine BFO. This finding is consistent with experimental bulk oxygen deficiencies (Y_{Fe}>Ce_{Fe}>La_{Ba}), determined by ubiodometric titration for the

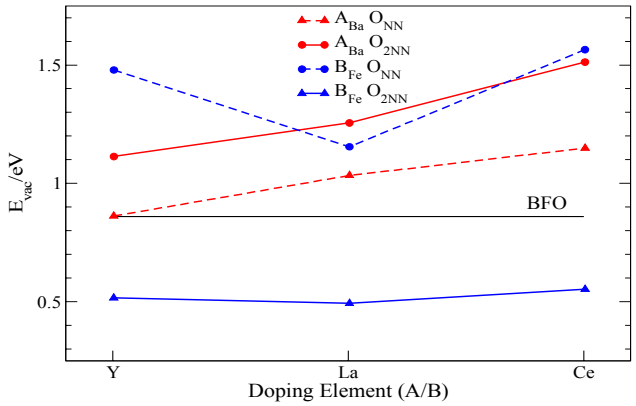

Figure 4. Energy required for oxygen vacancy formation for parent BFO (horizontal black line) and with A_{Ba} and B_{Fe} substitutions. O_{NN} and O_{2NN} vacancy energies are shown for distinct vacancy sites, as is Figure 1.

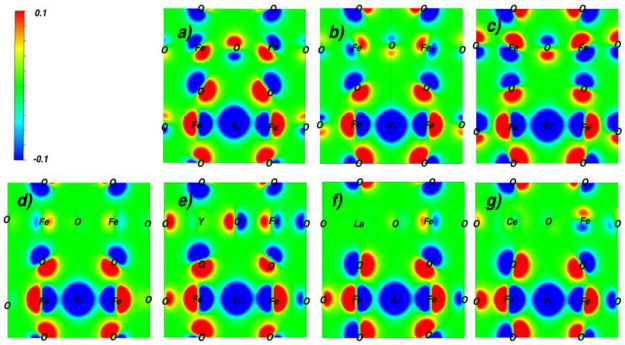

Figure 5. Charge density difference upon formation of an oxygen vacancy for the (100) plane: a) Y_{Ba}, b) La_{Ba}, c) Ce_{Ba}, d) BFO, e) Y_{Fe}, f) La_{Fe} and g) Ce_{Fe},. Positive charge corresponds to accumulation of electrons; negative charge corresponds to loss of electrons. $V_o^{\cdot\cdot}$ corresponds to oxygen vacancy: O_{NN}, vacancy site for A_{Ba}; and O_{2NN} vacancy site for B_{Fe}

single cubic phase structures.[27, 30, 32] However, as a consequence of the globally high energy of the B_{Fe} O_{NN} sites, it is expected that the improved oxygen deficiency will reach a limit for higher B_{Fe} substitution, as more O_{NN} sites will exist. This is a commonly observed trend for these materials and other substituted transition metal perovskites oxides.[25, 27, 32]

In summary, these findings suggest that B_{Fe}-substituted BFO may more easily form oxygen vacancies than A_{Ba} structures, yet with an upper limit due to the high energy of B_{Fe} defect-ordered vacancies.

3.5. Higher Oxygen Deficiency

As BFO and its derivatives have demonstrated high oxygen deficiencies, up to δ=0.38 (for iodometry at room temperature) La_{Ba}[25], the energy cost and mechanisms of additional oxygen vacancies were also explored for La_{Ba} and La_{Fe} defect structures. Bader charge redistribution for higher oxygen non-stoichiometry is also shown in Table 3. Interestingly for the formation of additional oxygen vacancies, the La_{Ba} substitution structure localises more donor charge to the oxygen sub-lattice. This is a similar mechanism to that observed for the La_{Fe} structure. Moreover, the additional localisation of charge per vacancy is of the same order for both La_{Ba} and La_{Fe} structures. This suggests a similar mechanism of donor accommodation for δ=0.25 and is supported by the comparable additional energy cost per additional vacancy (La_{Ba}: +0.20 eV and La_{Fe}: +0.22 eV). This is a reasonable observation because for both substitution and vacancy formation processes, similar charge redistribution processes occur, i.e. Fe reduction and O 2p donor localisation, yet in different orders. Interestingly for both La_{Ba} and La_{Fe} defects the magnetic moment of Fe increases with the oxygen vacancy level. Nonetheless, a higher oxygen deficiency is expected for La_{Fe} defects as they maintain a lower energy of formation for higher vacancy levels.

3.6 Electronic Conductivity

Analysing the DOS, shown in Figure 6, can give additional insight into the effect of oxygen deficiency and different site substitution on conductivity. Previous work has identified a correlation between the oxygen deficiency and temperature for La_{Ba} materials, showing an increased oxygen deficiency with temperature.[16] In addition, other work has identified an unusual trend for temperature and conductivity, where La_{Ba} materials (and other BFO materials)[21, 25] exhibit a semi-conductive behaviour for low temperatures, then transition to metallic conduction for intermediate temperatures and above (>450 °C).[16 62] Therefore, the electronic structures of La_{Ba} and La_{Fe} are analysed for different oxygen deficiencies to provide insight to these observations. A similar electronic structure dependence on the oxygen deficiency is observed for both types of La substitutions, suggesting that La_{Fe} may exhibit the same conduction type behaviour as observed for La_{Ba}. As shown in Figure 6 a transition from semi-metallic (conductor spin-up and insulator spin-down), to p-type semi-conductive back to semi-metallic, is observed for increasing oxygen deficiencies from δ=0.125, 0.25, 0.375. This suggests the material oxygen deficiency contributes to the experimental conduction observations.

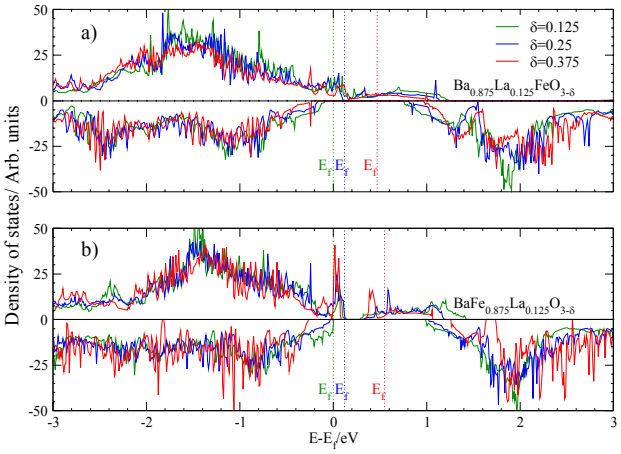

Figure 6 Total density of states for oxygen deficient BFO with a) La_{Ba} b) La_{Fe} substitutions, for oxygen deficiency δ=0.125, 0.25 & 0.375 with dashed lines corresponding to Fermi energy. The DOS have been aligned to the O2s core coincidence.

Further insight into the expected electronic conductivity mechanism can be gained by analysing the geometry of the doped structures. The mechanism of conductivity of perovskite type oxides is strongly correlated to the overlap of the O 2p and Fe 3d orbitals.[66] The extent of overlap of the O 2p and Fe 3d orbitals is characterised by the Fe-O bond distance (B-O) as detailed in Table 2, and Fe-O-Fe angle (B-O-B),[67] as detailed in Table 3. Firstly, a Fe-O bond expansion is observed for A_{Ba} and B_{Fe} substitution, with a direct impact on the Fe-O bond lengths, indicating a lower conductivity for stoichiometric B_{Fe} structures. Furthermore, for oxygen deficient structures, significant lattice torsion is observed for both defect types for both δ=0.125 and δ=0.25. However, for higher oxygen deficiencies, the lattice distortion for La_{Fe} defects is almost twice that of La_{Ba}. This finding, coupled with the expected higher oxygen deficiency for La_{Fe} defects, suggests that B_{Fe} doping will lead to lower conductivities.

The abovementioned features are consistent with experimental results for A_{Ba} and B_{Fe} defective structures, where a similar conduction transition from semi-conducting to metallic is observed for $Ba_{0.95}La_{0.05}FeO_{3-\delta}$ and $BaFe_{0.9}Y_{0.1}O_{3-\delta}$ at 450°C.[16, 30] In addition, the Y_{Fe} substituted material exhibited a lower conductivity compared to La_{Ba}.

3.7 Lattice Geometry

As previously outlined, stoichiometric expansion of the lattice is a key predictive tool for validating substitute site location. Here, the expected stoichiometric contraction and expansion associated to the ionic radii of the A_{Ba} and B_{Fe} defects respectively, was correctly observed, see Table 1. However, the expected stoichiometric expansion trend is not observed in the experimental data, as in Table 1. Indeed, in experiments a lattice expansion is observed for all dopants on both sites. This expansion is not expected for A_{Ba} substitution due to the lower ionic radii of the doping elements compared to Ba^{2+}. A reason

for this observation may be associated with the oxygen deficiency of the structures. The experimental BFO lattice constant is for the approximately stoichiometric structure (obtained using the ozone oxidation method[22]), whereas the A_{Ba} and B_{Fe} structures are all oxygen deficient (δ>0.25). Here, it was found that the creation of an oxygen vacancy produces a significant increase in the distance between the adjacent Fe ions (relative to the stoichiometric), 5-7%, Table 3. This local expansion is of a comparable level for both the parent BFO and the La_{Ba} and La_{Fe} substituted structures. The expansion is driven by the loss in electronic screening from the oxygen ion and consequent cation-cation repulsion, and has been identified in other DFT perovskite material analysis, yet to a much smaller extent. [44, 68] These results suggest that the oxygen vacancy induced local expansion is significant and a potential contributor to total lattice expansion. This finding may therefore explain the lattice expansion observed for the oxygen deficient A_{Ba} defect materials relative to the stoichiometric BFO.

As previously discussed, the introduction of substitutions into the parent BFO structure significantly affects the oxygen deficiency.[25] Therefore the local expansion due to oxygen deficiency may also provide insight into the total stoichiometric expansion when B_{Fe} defects are introduced into BFO. As previously outlined, the high energy of formation of O_{NN} vacancies as a consequence of B_{Fe} substitution may limit, and potentially reduce, the improved oxygen deficiency for higher substitution levels. Consequently, for larger substitution levels, oxygen reincorporation is expected, which will lead to a prominent local contraction, resulting from Fe-O-Fe interaction. This may in turn, dominate the ionic substitutional stoichiometric expansion, and may lead to an overall lattice contraction when increasing doping levels.

3.8 Substitution Defect Formation Energy

The above discussions have outlined the distinguishable characteristics of each site doping. However, as previously discussed, some materials in this study have yet to be fabricated. Therefore Table 4 shows the energetic cost of substitutional defect formation in the stoichiometric BFO, and hence the likelihood of formation for each site. The results suggest that La and Ce defects are more likely to occupy the Ba over Fe sites.[16, 21, 25, 27] For Y defects, Y_{Ba} exhibits the highest formation energy for A site substitution. This is plausible, given the small ionic radius of the Y cation, relative to Ba^{2+}. As a result, its small ionic radius may limit the coordination of elements to the Y_{Ba} site, which requires a 12-fold coordination. This may propose an additional energy barrier to formation. However, Y_{Fe} defects surprisingly exhibit a similar energy to $Y_{La,}$ which suggests an energy barrier to formation of the Y_{Fe} structure also. Indeed, the analysis of the charge redistribution reported in Table 2, suggests that in B_{Fe} defect formation the Fe cations are slightly reduced. This transitions the Fe into a less reducible state, increases the covalency of the Fe-O bond and facilitates better accommodation of charge in the oxygen lattice. However, the reduction of Fe^{3+} involves anti-parallel spin pairing, which contributes an additional energy barrier. Therefore, although B_{Fe} defects are less likely to form, if formation occurs, the charge redistribution is highly beneficial to further donor doping.

Table 4. Formation energy E_{form} (eV) for 12.5%, A_{Ba} and B_{Fe} substitutions in parent BFO.

	A_{Ba}	B_{Fe}
Y	1.44	1.43
La	0.29	2.11
Ce	1.36	2.56

3.9 Remarks

This DFT+U study modelled the structural effects associated with A_{Ba} and B_{Fe} substitutions in BFO and elucidated the mechanisms of electronic redistribution for substitute formation. Several site distinct characteristics were identified in good agreement with experimental observations, and it is envisaged that these findings may be employed to aid material design and development for SOFC cathode and oxygen transportation membrane applications. However, it is also essential to note that all findings introduced are limited to the DFT+U model employed. Therefore, this work serves to introduce the expected differences in properties and performance of the introduction of A_{Ba} and B_{Fe} into BFO and to highlight areas for further investigation. Furthermore, this suggests several key issues that should be extended by higher temperature and representative substitution level models.

4 Conclusions

This study has presented a detailed first principle DFT+U analysis of the electronic and quantum mechanical mechanisms of A_{Ba} and B_{Fe} substitutions (where A and B: Ce, Y, La) in BFO. Primarily, it is found that the substitution of each site A_{Ba} and $B_{Fe,}$ will have a very different effect on the lattice structure, oxygen deficiency and electronic conductivity. Charge analysis suggests that the accommodation of charge to the hole ordered O 2p orbitals in oxygen vacancy formation is essential for a low energy. Although B_{Fe} defects exhibit a high energy of formation, the charge redistribution in formation is favourable for later oxygen vacancy formation. Therefore, B_{Fe} defects are expected to facilitate a higher oxygen deficiency. However, a strong ionic nature of B_{Fe}-O_{NN} bonding for B_{Fe} structures is expected to limit the oxygen deficiency for higher substitution levels. Whereas for A_{Ba} defects, although more likely to occur, the effective donor doping results in a higher energy of formation of other donors (e.g. oxygen vacancies) and is expected to reduce the oxygen deficiency. A_{Ba} defects are also expected to exhibit a higher electronic conductivity, due to less lattice distortions for higher oxygen deficiency compared to B_{Fe} materials. In addition, oxygen deficiency is suggested as a prominent driver of stoichiometric expansion for both the parent BFO and A_{Ba} and B_{Fe} substituted structures, due to large adjacent Fe ion expansion and contraction for oxygen vacancy formation and reincorporation. This

observation provides physical insight into the unusual stoichiometric expansion trends for these materials.

Acknowledgements

The authors gratefully acknowledge the Research Grants Council of Hong Kong for support through the projects DAG12EG06 and ECS 639713. Zarah Medina Baiyee acknowledges the support of the Hong Kong PhD Fellowship Scheme.

References

1. J. R. Fanchi, *Energy: Technology and Directions for the Future*, Academic Press, 2004.
2. Z. Shao, S. M. Haile, J. Ahn, P. D. Ronney, Z. Zhan and S. A. Barnett, *Nature*, 2005, **435**, 795-798.
3. T. M. Gür, M. Homel and A. V. Virkar, *J. Power Sources*, 2010, **195**, 1085-1090.
4. E. P. Murray, T. Tsai and S. A. Barnett, *Nature*, 1999, **400**, 649-651.
5. E. D. Wachsman and K. T. Lee, *Science*, 2011, **334**, 935-939.
6. S. B. Adler, *Chem. Rev.*, 2004, **104**, 4791-4844.
7. I. Grinberg, D. V. West, M. Torres, G. Gou, D. M. Stein, L. Wu, G. Chen, E. M. Gallo, A. R. Akbashev, P. K. Davies, J. E. Spanier and A. M. Rappe, *Nature*, 2013, **503**, 509-512.
8. S. Colella, E. Mosconi, G. Pellegrino, A. Alberti, V. L. P. Guerra, S. Masi, A. Listorti, A. Rizzo, G. G. Condorelli, F. De Angelis and G. Gigli, *J. Phys. Chem. Lett.*, 2014, **5**, 3532-3538.
9. Z. Shao and S. M. Haile, *Nature*, 2004, **431**, 170-173.
10. T. Ishihara, S. Fukui, H. Nishiguchi and Y. Takita, *Solid State Ionics*, 2002, **152–153**, 609-613.
11. Y. Cheng, H. Zhao, D. Teng, F. Li, X. Lu and W. Ding, *J. Membr. Sci.*, 2008, **322**, 484-490.
12. H. Wang, C. Tablet, A. Feldhoff and J. Caro, *Adv. Mater.*, 2005, **17**, 1785-1788.
13. Z. Tao, L. Bi, Z. Zhu and W. Liu, *J. Power Sources*, 2009, **194**, 801-804.
14. S. McIntosh, J. F. Vente, W. G. Haije, D. H. A. Blank and H. J. M. Bouwmeester, *Chem. Mater.*, 2006, **18**, 2187-2193.
15. H. Lu, Y. Cong and W. S. Yang, *Solid State Ionics*, 2006, **177**, 595-600.
16. F. Dong, D. Chen, Y. Chen, Q. Zhao and Z. Shao, *J. Mater. Chem.*, 2012, **22**, 15071-15079.
17. Z. Shao, W. Yang, Y. Cong, H. Dong, J. Tong and G. Xiong, *J. Membr. Sci.*, 2000, **172**, 177-188.
18. D. Rembelski, J. P. Viricelle, L. Combemale and M. Rieu, *Fuel Cells*, 2012, **12**, 256-264.
19. W. T. Hong, M. Risch, K. A. Stoerzinger, A. Grimaud, J. Suntivich and Y. Shao-Horn, *Energy Environ. Sci.*, 2015, **8**, 1404-1427.
20. F. Dong, Y. Chen, D. Chen and Z. Shao, *ACS Appl. Mater. Interfaces*, 2014, **6**, 11180-11189.
21. W. D. Penwell and J. B. Giorgi, *Sens. Actuators, B*, 2014, **191**, 171-177.
22. N. Hayashi, T. Yamamoto, H. Kageyama, M. Nishi, Y. Watanabe, T. Kawakami, Y. Matsushita, A. Fujimori and M. Takano, *Angew. Chem.*, 2011, **123**, 12755-12758.
23. Y. Teraoka, H. Shimokawa, C. Kang, H. Kusaba and K. Sasaki, *Solid State Ionics*, 2006, **177**, 2245-2248.
24. C. Chen, D. Chen, Y. Gao, Z. Shao and F. Ciucci, *J. Mater. Chem. A*, 2014, **2**, 14154-14163.
25. X. Ding, X. Gao, W. Zhu, J. Wang and J. Jiang, *Int. J. Hydrogen Energy*, 2014, **39**, 12092-12100.
26. T. Kida, S. Ninomiya, K. Watanabe, N. Yamazoe and K. Shimanoe, *ACS Appl. Mater. Interfaces*, 2010, **2**, 2849-2853.
27. T. Kida, D. Takauchi, K. Watanabe, M. Yuasa, K. Shimanoe, Y. Teraoka and N. Yamazoe, *J. Electrochem. Soc.*, 2009, **156**, E187-E191.
28. T. Kida, A. Yamasaki, K. Watanabe, N. Yamazoe and K. Shimanoe, *J. Solid State Chem.*, 2010, **183**, 2426-2431.
29. D. Xu, F. Dong, Y. Chen, B. Zhao, S. Liu, M. O. Tade and Z. Shao, *J. Membr. Sci.*, 2014, **455**, 75-82.
30. X. Liu, H. Zhao, J. Yang, Y. Li, T. Chen, X. Lu, W. Ding and F. Li, *J. Membr. Sci.*, 2011, **383**, 235-240.
31. K. Watanabe, D. Takauchi, M. Yuasa, T. Kida, K. Shimanoe, Y. Teraoka and N. Yamazoe, *J. Electrochem. Soc.*, 2009, **156**, E81-E85.
32. X. Zhu, H. Wang and W. Yang, *Solid State Ionics*, 2006, **177**, 2917-2921.
33. X. Zhu, H. Wang and W. Yang, *Chem. Commun.*, 2004, **9**, 1130-1131.
34. S. R. Bishop, D. Marrocchelli, C. Chatzichristodoulou, N. H. Perry, M. B. Mogensen, H. L. Tuller and E. D. Wachsman, *Annu. Rev. Mater. Res.*, 2014, **44**, 205-239.
35. C. Chatzichristodoulou, P. Norby, P. V. Hendriksen and M. B. Mogensen, *J. Electroceram.*, 2014, **34**, 100-107.
36. V. V. Kharton, A. A. Yaremchenko, M. V. Patrakeev, E. N. Naumovich and F. M. B. Marques, *J. Eur. Ceram. Soc.*, 2003, **23**, 1417-1426.
37. A. M. Ritzmann, A. B. Muñoz-García, M. Pavone, J. A. Keith and E. A. Carter, *Chem. Mater.*, 2013, **25**, 3011-3019.
38. R. Pushpa, D. Daniel and D. P. Butt, *Solid State Ionics*, 2013, **249-250**, 184-190.
39. A. M. Ritzmann, A. B. Muñoz-García, M. Pavone, J. A. Keith and E. A. Carter, *MRS Commun.*, 2013, **3**, 161-166.
40. I. G. Joseph W. Bennett, and Andrew M. Rappe, *J. Am. Chem. Soc.*, 2008, **130**, 17409-17412.
41. F. Wang, I. Grinberg and A. M. Rappe, *Appl. Phys. Lett.*, 2014, **104**, 152903.
42. D. P. Kumah, A. Malashevich, A. S. Disa, D. A. Arena, F. J. Walker, S. Ismail-Beigi and C. H. Ahn, *Phys. Rev. Appl*, 2014, **2**.
43. Y.-L. Lee, J. Kleis, J. Rossmeisl, Y. Shao-Horn and D. Morgan, *Energy Environ. Sci.*, 2011, **4**, 3966-3970.
44. A. B. Muñoz-García, M. Pavone and E. A. Carter, *Chem. Mater.*, 2011, **23**, 4525-4536.
45. Y. A. Mastrikov, M. M. Kuklja, E. A. Kotomin and J. Maier, *Energy Environ. Sci.*, 2010, **3**, 1544.
46. Y. A. Mastrikov, R. Merkle, E. A. Kotomin, M. M. Kuklja and J. Maier, *Phys. Chem. Chem. Phys.*, 2013, **15**, 911-918.
47. R. Merkle, Y. A. Mastrikov, E. A. Kotomin, M. M. Kuklja and J. Maier, *J. Electrochem. Soc.*, 2012, **159**, B219.
48. G. Kresse and J. Furthmüller, *Phys. Rev. B*, 1996, **54**, 11169-11186.
49. J. P. Perdew, K. Burke and M. Ernzerhof, *Phys. Rev. Lett.*, 1997, **78**, 1396-1396.
50. H. J. Monkhorst and J. D. Pack, *Phys. Rev. B*, 1976, **13**, 5188-5192.
51. G. Kresse and D. Joubert, *Phys. Rev. B*, 1999, **59**, 1758-1775.
52. D. Andersson, S. Simak, B. Johansson, I. Abrikosov and N. Skorodumova, *Phys. Rev. B*, 2007, **75**, 035109.

53. F. Liang, K. Partovi, H. Jiang, H. Luo and J. Caro, *J. Mater. Chem. A*, 2013, **1**, 746-751.
54. L. Wang, T. Maxisch and G. Ceder, *Phys. Rev. B*, 2006, **73**, 195107.
55. Y.-L. Lee, J. Kleis, J. Rossmeisl and D. Morgan, *Phys. Rev. B*, 2009, **80**, 224101.
56. J. Janek, M. Martin and K. D. Becker, *Phys. Chem. Chem. Phys.*, 2009, **11**, 3010-3098.
57. B. Ribeiro, M. Godinho, C. Cardoso, R. P. Borges and T. P. Gasche, *J. Appl. Phys.*, 2013, **113**, 083906.
58. Z. Li, R. Laskowski, T. Iitaka and T. Tohyama, *Phys. Rev. B*, 2012, **85**, 134419.
59. R. F. W. Bader, *Acc. Chem. Res.*, 1985, **18**, 9-15.
60. W. Tang, E. Sanville and G. Henkelman, *J. Phys. Condens. Matter*, 2009, **21**, 084204.
61. M. Pavone, A. M. Ritzmann and E. A. Carter, *Energy Environ. Sci.*, 2011, **4**, 4933-4937.
62. R. D. Shannon, *Acta. Crystallogr. Sect. A*, 1976, **32**, 751-767.
63. L. Pauling, *The Nature of the Chemical Bond and the Structure of Molecules and Crystals: an Introduction to Modern Structural Chemistry*, Cornell University Press, 1960.
64. M. Mizumaki, K. Yoshii, N. Hayashi, T. Saito, Y. Shimakawa and M. Takano, *J. Appl. Phys.*, 2013, **114**, 073901.
65. C. E. Moore, *Ionization Potentials and Ionization Limits Derived From the Analyses of Optical Spectra*, DTIC Document, 1970.
66. P. H. T. Ngamou and N. Bahlawane, *Chem. Mater.*, 2010, **22**, 4158-4165.
67. Y. Guo, H. Shi, R. Ran and Z. Shao, *Int. J. Hydrogen Energy*, 2009, **34**, 9496-9504.
68. A. S. Ogale, S. B. Ogale, R. Ramesh and T. Venkatesan, *Appl. Phys. Lett.*, 1999, **75**, 537-539.

1